JM PAPERS

A hybrid pseudo-incompressible–hydrostatic model

A.P. Snodin[1] and T.S. Wood[1],†

[1]School of Mathematics, Statistics and Physics, Newcastle University, Newcastle on Tyne NE1 7RU, UK

The pseudo-incompressible approximation, which assumes small pressure perturbations from a one-dimensional reference state, has long been used to model large-scale dynamics in stellar and planetary atmospheres. However, existing implementations do not conserve energy when the reference state is time-dependent. We use a variational formulation to derive an energy-conserving pseudo-incompressible model in which the reference state evolves while remaining hydrostatic. We present an algorithm for solving these equations in the case of closed boundaries, for which the pseudo-incompressible velocity constraint is degenerate. We implement the model within the low-Mach-number code MAESTROeX, and validate it against a fully compressible model in several test cases, finding that our hybrid pseudo-incompressible–hydrostatic model generally shows better agreement with the compressible results than the existing MAESTROeX implementation.

Key words: atmospheric flows, stratified flows, variational methods

1. Introduction

In a wide variety of fluid dynamical systems sound waves play no significant role on the time and length scales of interest. Yet their presence generally requires them to be resolved in numerical calculations in order to maintain numerical stability. For explicit numerical schemes, the time step Δt cannot exceed $\Delta x / \max\{c, u\}$, where Δx is the smallest scale resolved in the simulation, c is the sound speed and u is the magnitude of the fluid velocity. For flows of very low Mach number, i.e. flows with $u \ll c$, this imposes an impracticable limit on the numerical time step. So-called 'sound-proof' models explicitly remove sound waves from the equations that are solved, so that the time step is no longer constrained by the sound speed. In practical applications this may result in a reduction in computational time by several orders of magnitude. Various sound-proof models have been derived for

† Email address for correspondence: toby.wood@ncl.ac.uk

different applications, each of which requires particular physical assumptions and has its own domain of validity.

A completely different approach is to solve the fully compressible equations using an implicit (or semi-implicit) numerical scheme, which avoids the need for very small computational time steps (e.g. Viallet *et al.* 2016). However, such methods do not remove sound waves from the dynamics; rather they introduce numerical dissipation that prevents sound waves from growing to significant amplitudes. To minimise the effect of this numerical dissipation on the results, such models use preconditioning techniques that are tailored to the particular problem of interest (Goffrey *et al.* 2017).

Of the various sound-proof approximations, the pseudo-incompressible approximation has the advantage that it can be derived under a single assumption: that the (Eulerian) pressure perturbations are small (Durran 1989, 2008; Vasil *et al.* 2013). In particular, Vasil *et al.* (2013) have shown that the pseudo-incompressible equations can be obtained by applying Hamilton's principle to a suitable action, which is obtained simply by linearising the pressure variable about a given 'background' field, P_0. Although the resulting equations describe only ideal (i.e. adiabatic) dynamics, they can be extended to include non-ideal processes by invoking 'thermodynamic consistency' (Klein & Pauluis 2012), or by using an extended variational principle (Gay-Balmaz 2019). The main advantage of using a variational formalism is that it guarantees (via Noether's theorem) that the equations obey conservation laws that are directly analogous to those of the unapproximated system.

In the simplest implementation of the pseudo-incompressible approximation, the background pressure, P_0, is a fixed function of altitude. However, the resulting equations have two shortcomings:

(i) they become inaccurate on large horizontal scales (for which pressure perturbations are significant e.g. Davies *et al.* 2003); and

(ii) they imply a constraint on the velocity field that cannot generally be maintained in the presence of heat sources, at least for certain choices of the boundary conditions (e.g. Rehm & Baum 1978; Lecoanet *et al.* 2014).

For these reasons, and for the sake of greater generality, it is desirable to allow the background pressure field to evolve in time, whilst maintaining hydrostatic balance (Almgren 2000; Almgren *et al.* 2008; O'Neill & Klein 2014). We refer to this as the hybrid pseudo-incompressible–hydrostatic model. However, by allowing the background pressure to evolve we violate one of the assumptions under which the variational derivations were performed, and as a result the hybrid model generally does not maintain exact energy conservation.

The purpose of this paper is to resolve this problem by generalising the method of Vasil *et al.* (2013) to allow the background pressure P_0 to vary in time, subject to the constraint that the horizontally averaged dynamics is hydrostatic. To enforce this additional constraint, we introduce an additional Lagrange multiplier into the fluid action, which results in an additional force in the momentum equation. (Such a force is expected whenever an additional constraint is imposed, though this point does not always seem to have been recognised in the literature.) As a proof of concept we present an implementation of our hybrid equations using the MAESTROeX code (Fan *et al.* 2019*a*).

We note that an alternative hybrid model can be obtained by generalising the hydrostatic approximation (Miller & Pearce 1974; White 1989; Arakawa & Konor 2009), and a variational formalism has already been used to obtain 'quasi-hydrostatic' and 'semi-hydrostatic' approximations (Salmon & Smith 1994; Dubos & Voitus 2014).

Such approximations are well suited to many meteorological applications, in which the dynamics occurs on large horizontal scales (measured relative to a typical vertical scale height). However, the pseudo-incompressible approximation is generally more accurate for modelling dynamics on small horizontal length scales, such as atmospheric convection and other buoyancy processes, which form the motivation for the present work.

2. The constrained fluid action

2.1. *The fully compressible fluid*

To obtain the equations of motion using Hamilton's principle, we first need to identify the appropriate action for the dynamical system in question. For a fluid, the most natural representation of the action is in terms of Lagrangian coordinates (Salmon 1988). However, in applications it is far more convenient to express the equations in Eulerian form, and so in what follows we take the standard 'hybrid Lagrangian–Eulerian' approach (Bretherton 1970). The action is expressed in Eulerian form as the space–time integral

$$S = \iint \mathcal{L} \, \mathrm{d}^3x \, \mathrm{d}t, \tag{2.1}$$

where $\mathcal{L}$ is the Lagrangian density, the most concise form of which for a fully compressible fluid is

$$\mathcal{L} = \tfrac{1}{2}\rho|\boldsymbol{u}|^2 - \rho\Phi - \rho U(\rho, s). \tag{2.2}$$

Here, ρ is the fluid density, $\boldsymbol{u}$ is the velocity, Φ is the gravitational potential and U is the specific internal energy, which is naturally a function of the density and specific entropy, s. We make the Cowling approximation by assuming that Φ is a given function of space only, although the method can be generalised to include self-gravity if required. We now calculate the first variation of the action with respect to the fields ρ, s and $\boldsymbol{u}$:

$$\delta S = \iint \left[\left(\frac{1}{2}|\boldsymbol{u}|^2 - \Phi - U - \rho\frac{\partial U}{\partial \rho} \right) \delta\rho + \rho\boldsymbol{u} \cdot \delta\boldsymbol{u} - \rho\frac{\partial U}{\partial s} \delta s \right] \mathrm{d}^3x \, \mathrm{d}t. \tag{2.3}$$

The variations δS, $\delta\rho$ and $\delta\boldsymbol{u}$ are not independent, since they all result from the same variation in the fluid element trajectories. We can express each of them in terms of the Lagrangian displacement, $\boldsymbol{\xi}$, as follows (Newcomb 1962):

$$\delta\rho = -\nabla \cdot (\rho\boldsymbol{\xi}), \quad \delta s = -\boldsymbol{\xi} \cdot \nabla s, \quad \delta\boldsymbol{u} = \frac{\partial \boldsymbol{\xi}}{\partial t} + \boldsymbol{u} \cdot \nabla\boldsymbol{\xi} - \boldsymbol{\xi} \cdot \nabla\boldsymbol{u}. \tag{2.4a–c}$$

From these expressions, and integrating by parts, we can write the first variation of the action as

$$\delta S = -\iint \rho\boldsymbol{\xi} \cdot \left(\frac{\mathrm{D}\boldsymbol{u}}{\mathrm{D}t} + \nabla\Phi + \frac{1}{\rho}\nabla P \right) \mathrm{d}^3x \, \mathrm{d}t, \tag{2.5}$$

where

$$\frac{\mathrm{D}}{\mathrm{D}t} \equiv \frac{\partial}{\partial t} + \boldsymbol{u} \cdot \nabla \tag{2.6}$$

represents the usual Lagrangian derivative and P is the fluid pressure:

$$P = P_{EoS}(\rho, s) \equiv \rho^2 \left(\frac{\partial U}{\partial \rho} \right)_s. \tag{2.7}$$

We use the subscript 'EoS' to indicate a quantity that can be expressed explicitly as a function of ρ and s via an equation of state.

Hamilton's principle states that $\delta\mathcal{S}$ must vanish for all possible choices of $\boldsymbol{\xi}$, and hence we obtain the usual Euler equation:

$$\frac{\mathrm{D}\boldsymbol{u}}{\mathrm{D}t} = -\nabla\Phi - \frac{1}{\rho}\nabla P. \tag{2.8}$$

Moreover, the forms assumed for $\delta\rho$ and δs in (2.4a–c) guarantee the conservation of mass and entropy, so we also have

$$\frac{\partial\rho}{\partial t} = -\nabla\cdot(\rho\boldsymbol{u}) \quad \text{and} \quad \frac{\mathrm{D}s}{\mathrm{D}t} = 0. \tag{2.9a,b}$$

Since the action contains no explicit time dependence, it follows from Noether's theorem that the system conserves a total energy, whose density, E say, we can deduce easily from the action:

$$E = \tfrac{1}{2}\rho|\boldsymbol{u}|^2 + \rho\Phi + \rho U. \tag{2.10}$$

We note that the correct definition of the fluid pressure, given by (2.7), follows directly from the derivation. By contrast, since the dynamics arising from Hamilton's principle is necessarily adiabatic, we have not needed to define the fluid temperature. However, the correct definition can be deduced by requiring that the laws of thermodynamics are obeyed. Specifically, in the presence of a volumetric heat source, Q, we expect the fluid entropy to obey a prognostic equation of the form

$$\frac{\mathrm{D}s}{\mathrm{D}t} = \frac{Q}{\rho T}, \tag{2.11}$$

and the temperature, T, must be defined such that the energy, E, remains a conserved quantity; Klein & Pauluis (2012) refer to this as the principle of 'thermodynamic consistency'. In the case of a fully compressible fluid this leads, of course, to the usual definition:

$$T = T_{EoS}(\rho, s) \equiv \left(\frac{\partial U}{\partial s}\right)_\rho. \tag{2.12}$$

2.2. *The pseudo-incompressible fluid*

As shown by Vasil *et al.* (2013), the pseudo-incompressible approximation can be obtained in a general form simply by supplementing the Lagrangian density $\mathcal{L}$ with an additional term

$$-\lambda(P_{EoS} - P_0). \tag{2.13}$$

Here, $P_{EoS}(\rho, s)$ is defined as previously, $P_0(\boldsymbol{x})$ is a prescribed background pressure and $\lambda(\boldsymbol{x}, t)$ is a Lagrange multiplier. When Hamilton's principle is applied, λ is regarded as an additional, independent variable, and therefore serves to enforce the constraint $P_{EoS} = P_0$. This constraint implies that the density, and hence the volume, of each fluid element depends entirely on its entropy and its Eulerian position, without any reference to pressure perturbations. In this way, acoustic waves are removed from the system (Durran 2008).

As discussed in the Introduction, the 'generalised pseudo-incompressible' equations obtained by Vasil *et al.* (2013) can be extended to include diabatic processes by invoking thermodynamic consistency. However, if the background pressure P_0 is still regarded as a fixed function of space only, then the resulting equations become ill-posed for certain

boundary conditions. To see why, we take the Lagrangian derivative of the constraint equation $P_{EoS}(\rho, s) = P_0(\boldsymbol{x})$, which tells us that

$$\frac{\partial P_{EoS}}{\partial \rho} \frac{\mathrm{D}\rho}{\mathrm{D}t} + \frac{\partial P_{EoS}}{\partial s} \frac{\mathrm{D}s}{\mathrm{D}t} = \boldsymbol{u} \cdot \nabla P_0. \tag{2.14}$$

Using mass conservation and the diabatic heating equation (2.11), this becomes

$$\rho c^2 \nabla \cdot \boldsymbol{u} + \boldsymbol{u} \cdot \nabla P_0 = \frac{\partial^2 U}{\partial s \partial \rho} \frac{\rho Q}{T}, \tag{2.15}$$

where $c^2(\rho, s) \equiv \partial P_{EoS}/\partial \rho$ is the square of the sound speed. If, for example, Q represents an external injection of heat into the fluid, then we expect the right-hand side of this equation to be positive. This implies that the left-hand side must also be positive, and hence the fluid must expand. But if we impose impenetrable boundary conditions over the entire surface of the fluid, then expansion in any region of the fluid must be balanced by contraction elsewhere, which is not compatible with (2.15). The obvious solution to this problem is to allow the pressure P_0 to change in response to heating, and as described in the Introduction this has long been recognised in numerical implementations of the pseudo-incompressible approximation. A further advantage of allowing the background state to evolve is that it is more self-consistent, and leads to a more 'universal' model that is free from any imposed background profiles. But if P_0 is allowed to vary in time then there is no longer any reason to expect the model to conserve energy.

2.3. *The hybrid pseudo-incompressible–hydrostatic model*

Our goal is to generalise the derivation of Vasil *et al.* (2013) to allow the background pressure to evolve, but subject to the condition that it remains horizontally invariant, and hydrostatic. At the level of the action, we can enforce this as a constraint by supplementing the Lagrangian density with a term

$$\mu \left(\frac{\partial}{\partial z} P_{EoS} - g\rho \right), \tag{2.16}$$

where for simplicity we have assumed a plane-parallel atmosphere, with uniform gravitational acceleration $\boldsymbol{g} = -\nabla \Phi = g\boldsymbol{e}_z$. (We use the convention that g is negative.) A similar constraint has previously been used to derive a 'semi-hydrostatic' model (Dubos & Voitus 2014), but the difference here is that we only wish to impose this constraint on the horizontally averaged fields. We therefore take the Lagrange multiplier μ to be horizontally invariant, i.e. $\mu(z, t)$, so that the constraint it enforces is

$$\frac{\partial}{\partial z} \overline{P_{EoS}} = g\bar{\rho}, \tag{2.17}$$

where an overbar represents a horizontal average. Since we still want to make the pseudo-incompressible approximation, we simultaneously enforce the constraint

$P_{EoS} = \overline{P_{EoS}}$. Thus, our pseudo-incompressible–hydrostatic action has the form

$$\mathcal{S} = \iint \left[\frac{1}{2}\rho|\boldsymbol{u}|^2 + gz\rho - \rho U - (\lambda - \bar{\lambda})P_{EoS} + \mu \left(\frac{\partial}{\partial z}P_{EoS} - g\rho \right) \right] \mathrm{d}^3\boldsymbol{x}\,\mathrm{d}t, \quad (2.18)$$

where we have used the fact that

$$\int \lambda\overline{P_{EoS}}\,\mathrm{d}^3\boldsymbol{x} = \int \bar{\lambda}P_{EoS}\,\mathrm{d}^3\boldsymbol{x} \qquad (2.19)$$

to remove any explicit reference to $\overline{P_{EoS}}$ from the action. We note that the action (2.18) only depends on the non-horizontally averaged part of λ, that is $(\lambda - \bar{\lambda})$, and so $\bar{\lambda}$ is essentially arbitrary; we will take advantage of this fact shortly.

It is now straightforward to obtain the equations of motion via Hamilton's principle, which leads to the following momentum equation:

$$\rho \left(\frac{\mathrm{D}\boldsymbol{u}}{\mathrm{D}t} + \frac{1}{\rho}\nabla P_{EoS} - g\nabla(z - \mu) \right) = \left(\lambda - \bar{\lambda} + \frac{\partial\mu}{\partial z} \right)\nabla P_{EoS} - \nabla\left[\left(\lambda - \bar{\lambda} + \frac{\partial\mu}{\partial z} \right)\rho c^2 \right]. \qquad (2.20)$$

Given that the horizontal average of λ is essentially arbitrary, we can simplify this result by declaring that $\bar{\lambda} = \partial\mu/\partial z$. Our complete set of equations is then

$$\rho\frac{\mathrm{D}\boldsymbol{u}}{\mathrm{D}t} = (1 - \bar{\lambda})\rho\boldsymbol{g} - (1 - \lambda)\nabla P - \nabla(\lambda\rho c^2), \qquad (2.21)$$

$$\frac{\partial\rho}{\partial t} = -\nabla \cdot (\rho\boldsymbol{u}), \qquad (2.22)$$

$$\frac{\mathrm{D}s}{\mathrm{D}t} = 0, \qquad (2.23)$$

$$\nabla P = \bar{\rho}\boldsymbol{g}, \qquad (2.24)$$

where, for brevity, we use the symbol P to refer to both P_{EoS} and its horizontal average, which are equal by construction. From this point onwards, it is more convenient to regard $P(z, t)$ as an independent variable, alongside $\rho(\boldsymbol{x}, t)$, rather than as a function of ρ and s. We will therefore henceforth regard the quantities s and c as functions of P and ρ, and for later convenience we introduce the quantity

$$s_P \equiv \left(\frac{\partial s}{\partial P} \right)_\rho. \qquad (2.25)$$

We note that our momentum equation (2.21) differs from that of Vasil *et al.* (2013) and Klein & Pauluis (2012) only in the presence of $\bar{\lambda}$, which serves to modify the effective gravitational field. As in the model of Dubos & Voitus (2014), it is possible to interpret μ (and hence $\bar{\lambda}$) as a correction to the geopotential height.

As mentioned earlier, a major advantage of having made all of our approximations at the level of the action is that the model is guaranteed to admit conservation laws similar to those of the exact system, provided that our approximations do not violate the relevant mathematical symmetries. In particular, the additional constraint terms in (2.18) do not explicitly depend on either position or time, and so our hybrid model is guaranteed to conserve momentum and energy in some form. Another conserved quantity, which is of central importance in meteorology, is the potential vorticity, which owes its existence to the indistinguishability of fluid particles lying within surfaces of constant entropy

(Salmon 1982). In terms of our Lagrangian–Eulerian description, it can be shown that potential vorticity is a materially conserved quantity provided that the first variation of the action depends on $\boldsymbol{\xi}$ only through $\delta\rho$, δs and $\delta\boldsymbol{u}$ (Vasil *et al.* 2013). This result can also be derived directly from our momentum equation (2.21), whose curl yields the vorticity equation

$$\frac{\partial\boldsymbol{\omega}}{\partial t} - \boldsymbol{\nabla}\times(\boldsymbol{u}\times\boldsymbol{\omega}) = \boldsymbol{\nabla}\left(T_{EoS} + \frac{\lambda}{\rho\,s_P}\right)\times\boldsymbol{\nabla}s, \tag{2.26}$$

where $\boldsymbol{\omega}\equiv\boldsymbol{\nabla}\times\boldsymbol{u}$ is the vorticity. Because the right-hand side here is perpendicular to $\boldsymbol{\nabla}s$, it follows that the circulation around any isentropic material curve remains constant in time, and hence that the quantity

$$q \equiv \frac{\boldsymbol{\omega}\cdot\boldsymbol{\nabla}s}{\rho} \tag{2.27}$$

is materially conserved.

2.4. *Thermodynamic consistency*

As just mentioned, (2.21)–(2.24) are guaranteed to conserve energy in some form. In fact, since the action (2.18) only differs from the fully compressible action by constraint terms, the conserved energy must have exactly the form given by (2.10). Indeed, using (2.21)–(2.24) it can be shown that

$$\frac{\partial E}{\partial t} + \boldsymbol{\nabla}\cdot\left[(E+P+\lambda\rho c^2+\rho g\mu)\boldsymbol{u} + \frac{\partial P}{\partial t}\mu\boldsymbol{e}_z\right] = -g\mu\frac{\partial}{\partial t}(\rho-\bar{\rho}) - (\lambda-\bar{\lambda})\frac{\partial P}{\partial t}. \tag{2.28}$$

This result demonstrates that E is no longer a locally conserved quantity in our hybrid approximation, i.e. it does not satisfy a local conservation law, unless the right-hand side happens to be zero. However, the right-hand side has zero horizontal average, and so the horizontally averaged energy, $\bar{E}$, is still a conserved quantity, i.e. it does satisfy a local conservation law. In other words, imposing hydrostatic balance causes energy to be instantaneously redistributed within each horizontal surface, but energy is still conserved locally in the vertical direction, and hence also globally.

We emphasise that in order to obtain this result, we needed to use the momentum equation (2.21), which includes an additional force not present in previous pseudo-incompressible models (e.g. Durran 1989; Almgren *et al.* 2008; Klein & Pauluis 2012; Vasil *et al.* 2013; O'Neill & Klein 2014; Fan *et al.* 2019a). The presence of this force follows directly from Hamilton's principle.

Another important feature of (2.28) is that it contains additional energy flux terms compared with the fully compressible energy equation. The first of these, $\lambda\rho c^2$, was already present in previous pseudo-incompressible models, where it was identified as a pressure perturbation and often denoted as p' or π. The other terms involve our new Lagrange multiplier μ and therefore have not previously arisen. Their contribution to the total energy budget can be made to vanish by imposing either that $\mu=0$ or that $\partial P/\partial t = -g\overline{\rho u_z}$ on the upper and lower boundaries. As we show in § 3, the latter is appropriate if the domain has open boundaries, whereas the former is required for a closed domain.

We now invoke thermodynamic consistency to identify the appropriate definition of the temperature in our hybrid model. If we replace the adiabatic heat equation (2.23) with its diabatic counterpart (2.11), we find that the energy equation (2.28) now acquires an

additional source term on its right-hand side,

$$\left[T_{EoS} + \frac{\lambda}{\rho \, s_P} \right] \frac{Q}{T}, \tag{2.29}$$

but is otherwise unchanged. To preserve the first law of thermodynamics, we must therefore define the temperature to be

$$T \equiv T_{EoS} + \frac{\lambda}{\rho \, s_P}. \tag{2.30}$$

The same result was obtained by Klein & Pauluis (2012) and Gay-Balmaz (2019). We emphasise that, since this formula for T depends on the quantity λ, the 'correct' temperature cannot generally be obtained from the usual equation of state.

2.5. *The velocity constraint and solvability*

In summary, our diabatic equations are

$$\rho \frac{D\boldsymbol{u}}{Dt} = (1 - \bar{\lambda})\rho\boldsymbol{g} - (1 - \lambda)\nabla P - \nabla(\lambda\rho c^2), \tag{2.31}$$

$$\frac{\partial \rho}{\partial t} = -\nabla \cdot (\rho\boldsymbol{u}), \tag{2.32}$$

$$\frac{Ds}{Dt} = \frac{Q}{\rho T}, \tag{2.33}$$

$$\nabla P = \bar{\rho}\boldsymbol{g}, \tag{2.34}$$

$$T = T_{EoS} + \frac{\lambda}{\rho \, s_P}. \tag{2.35}$$

Although the set of (2.31)–(2.35) is complete, for the sake of obtaining solutions it is convenient to rearrange them a little. First, the heat equation (2.33) can be expressed as an evolution equation for P:

$$\frac{\partial P}{\partial t} + \boldsymbol{u} \cdot \nabla P = -\rho c^2 \nabla \cdot \boldsymbol{u} + \frac{Q}{\rho T \, s_P}. \tag{2.36}$$

However, only the horizontally averaged part of this equation is required to evolve P, and the rest serves as a constraint on the velocity. An alternative equation for $\partial P/\partial t$ can be obtained by taking the Eulerian time derivative of the hydrostatic constraint (2.34). Using the continuity equation (2.32), and assuming periodic or impenetrable side boundaries and an impenetrable lower boundary, we find that

$$\frac{\partial}{\partial z} \frac{\partial P}{\partial t} = -g \frac{\partial}{\partial z} \overline{\rho u_z}$$

$$\Rightarrow \quad \frac{\partial P}{\partial t} = -g\overline{\rho u_z} + \dot{P}_b, \tag{2.37}$$

where $\dot{P}_b(t)$ is the rate of change of the pressure on the lower boundary. This function will depend on the choice of boundary condition at the upper boundary. For example, in the

936 A14-8

case where the upper boundary is impenetrable it is convenient to eliminate $\partial P/\partial t$ between (2.36) and (2.37), leading to a constraint equation for the velocity field:

$$\frac{g}{\rho c^2}(\bar{\rho}u_z - \overline{\rho u_z}) + \boldsymbol{\nabla} \cdot \boldsymbol{u} = S - \frac{\dot{P}_b}{\rho c^2}, \qquad (2.38)$$

where we have defined

$$S \equiv \frac{1}{\rho^2 c^2 \, s_P} \frac{Q}{T} \qquad (2.39)$$

to match the notation used in the low-Mach-number literature (Fan *et al.* 2019*a*). If we neglect the $\dot{P}_b$ term here then in general this equation has no solutions that meet the impenetrable boundary conditions; this is just an example of the problem mentioned in § 2.2, and indicates that the velocity constraint is degenerate for this choice of boundary conditions. The correct value for $\dot{P}_b$ must therefore be obtained as a solvability condition for (2.38). For example, if the horizontal average of the first term in (2.38) can be neglected, then taking the volume average of this equation we deduce that

$$\dot{P}_b \simeq \frac{\int_V S \, \mathrm{d}^3\boldsymbol{x}}{\int_V 1/(\rho c^2) \, \mathrm{d}^3\boldsymbol{x}} \qquad (2.40)$$

(O'Neill & Klein 2014). An alternative scenario, more relevant to atmospheric applications, is that of a semi-infinite atmosphere with an impenetrable lower boundary. Since the total mass of the semi-infinite atmosphere remains constant, and is assumed to remain in hydrostatic balance, it is arguable that the pressure on the lower boundary should remain approximately constant, i.e. that $\dot{P}_b \simeq 0$ (Almgren 2000). This assumption is implicit in the MAESTROeX model, which neglects the function $\dot{P}_b$ (Almgren *et al.* 2008), although in practice the equations are solved in a finite computational domain, and the upper boundary is taken either to be impenetrable or to have a fixed pressure. Furthermore (2.40) shows that, even in the limit of a semi-infinite atmosphere, we obtain $\dot{P}_b = 0$ only if the injected heat, Q, vanishes sufficiently rapidly with height.

In both of the cases just described, we arrive at an approximate expression for the function $\dot{P}_b$. Because the result is only approximate, if we use it we must necessarily abandon (at least) one of the 'exact' (2.31)–(2.34). For example, O'Neill & Klein (2014) chose to abandon hydrostatic balance and/or mass conservation in their model. (More precisely, they allowed the 'pseudo-density', which satisfies the continuity equation, to depart from the 'background density', which satisfies hydrostatic balance). In the MAESTROeX model, which assumes that $\dot{P}_b = 0$, the heat equation (2.33) is not used.

In the next section we describe a more consistent procedure for determining the value of $\dot{P}_b$, and how this can be implemented within the existing framework of the MAESTROeX code. For definiteness we focus on the case of a closed domain, in which the upper and lower boundaries are both impenetrable, so that the total energy ought to be conserved.

3. The solution procedure

To avoid inessential complications, in what follows we consider an ideal gas, so that the relations between the thermodynamic variables can be stated explicitly. Our complete set

of equations is then

$$\rho \frac{\mathrm{D}\boldsymbol{u}}{\mathrm{D}t} = (\rho - \bar{\rho} - \bar{\lambda}\rho)\boldsymbol{g} - P^{1/\gamma}\boldsymbol{\nabla}(\gamma P^{1-1/\gamma}\lambda), \tag{3.1}$$

$$\frac{\partial \rho}{\partial t} = -\boldsymbol{\nabla}\cdot(\rho\boldsymbol{u}), \tag{3.2}$$

$$\boldsymbol{\nabla}P = \bar{\rho}\boldsymbol{g}, \tag{3.3}$$

$$\gamma P\boldsymbol{\nabla}\cdot\boldsymbol{u} + \boldsymbol{u}\cdot\boldsymbol{\nabla}P - g\overline{\rho u_z} = \gamma PS - \dot{P}_b, \tag{3.4}$$

$$S = \frac{Q/(\gamma P)}{\dfrac{1}{\gamma - 1} + \lambda}. \tag{3.5}$$

The MAESTROeX code (Fan *et al.* 2019*a*,*b*) is a massively parallel, finite-volume solver for low-Mach-number astrophysical flows. It allows us to solve the above equations after having modified the code to include the terms involving $\bar{\lambda}$ and $\dot{P}_b$ for planar geometry (avoiding the additional complexity of the spherical implementation for now). It also allows for adaptive mesh refinement and reactions between multiple species, but we do not consider those features here. Although we only consider an ideal gas here, our changes to the code have been implemented for an arbitrary equation of state.

The code uses a predictor–corrector scheme, in which most quantities are updated several times over the course of a single time step. However, for our purposes the essential steps of the algorithm are:

(i) Timestep the momentum equation (3.1) using an 'old' value of λ.
(ii) Calculate the necessary correction to λ and $\boldsymbol{u}$ in order to meet the velocity constraint (3.4).
(iii) Timestep the continuity equation (3.2).
(iv) Update the pressure by integrating the hydrostatic balance equation (3.3).

The critical step here is determining the correction to λ (which in practice is only updated at the end of each time step). Suppose that the 'true' value of λ is larger than the old value by $\Delta\lambda$. Then the velocity we initially obtain after taking a time step of size Δt will be

$$\boldsymbol{u}^{\dagger} = \boldsymbol{u} + \frac{P^{1/\gamma}}{\rho}\boldsymbol{\nabla}\phi + \frac{\bar{\phi}}{\gamma P^{1-1/\gamma}}\boldsymbol{g}, \tag{3.6}$$

where $\boldsymbol{u}$ represents the 'true' velocity, and where we have defined $\phi \equiv \gamma P^{1-1/\gamma}\,\Delta\lambda\,\Delta t$. Substituting this into the velocity constraint (3.4), we obtain the following equation for ϕ:

$$\boldsymbol{\nabla}\cdot\left(\frac{P^{2/\gamma}}{\rho}\boldsymbol{\nabla}\phi\right) - \frac{(\gamma-1)gP^{2/\gamma}}{\gamma^2 P^2}\frac{\partial P}{\partial z}\bar{\phi} = \boldsymbol{\nabla}\cdot(P^{1/\gamma}\boldsymbol{u}^{\dagger}) - \frac{gP^{1/\gamma}}{\gamma P}\overline{\rho u_z^{\dagger}} - \frac{\gamma PS - \dot{P}_b}{\gamma P^{1-1/\gamma}}. \tag{3.7}$$

In Appendix A we describe how this equation can be solved, by formulating its adjoint problem, and the associated solvability condition for $\dot{P}_b$. However, since implementing this would require significant changes to the existing MAESTROeX algorithm, we here present an approximate solution procedure that is more in keeping with the existing code. We also note that MAESTROeX uses a slightly different definition for the quantity ϕ, which has been found to improve numerical stability (Almgren, Bell & Crutchfield 2000; Almgren *et al.* 2008) but is mathematically equivalent to what we present here.

Currently, MAESTROeX actually implements the velocity constraint in two parts, by writing the density and velocity fields as the sums of horizontally averaged and remainder contributions: $\rho = \bar{\rho} + \tilde{\rho}$ and $\boldsymbol{u} = \overline{u_z}\boldsymbol{e}_z + \tilde{\boldsymbol{u}}$. The velocity constraint (3.4) can then be separated into two equations:

$$\gamma P \frac{\partial}{\partial z}\overline{u_z} - g\overline{\tilde{\rho}\tilde{u}_z} = \gamma P\bar{S} - \dot{P}_b, \tag{3.8}$$

$$\nabla \cdot (P^{1/\gamma}\tilde{\boldsymbol{u}}) = P^{1/\gamma}(S - \bar{S}). \tag{3.9}$$

Equation (3.8) is solved for $\overline{u_z}$ by integrating upward from the lower boundary, and using an 'old' value of $\overline{\tilde{\rho}\tilde{u}_z}$. The quantity $\dot{P}_b$ is currently neglected in this calculation, which means that the solution cannot generally be made to satisfy an impenetrable upper boundary condition. In order to allow for impenetrable boundaries above and below, we must take

$$\dot{P}_b = \frac{\int \left[S + g\tilde{\rho}\tilde{u}_z/(\gamma P)\right] \mathrm{d}^3\boldsymbol{x}}{\int 1/(\gamma P)\,\mathrm{d}^3\boldsymbol{x}}, \tag{3.10}$$

which is a straightforward generalisation of the result (2.40) used by O'Neill & Klein (2014). The value of $\dot{P}_b$ obtained here can then be used later for the lower boundary condition in step (iv) of the algorithm described above. After $\overline{u_z}$ is calculated from (3.8), we can substitute (3.6) into (3.9), which leads to the following equation for ϕ:

$$\nabla \cdot \left(\frac{P^{2/\gamma}}{\rho}\nabla\phi\right) = \nabla \cdot \left(P^{1/\gamma}\left(\boldsymbol{u}^{\dagger} - \overline{u_z}\boldsymbol{e}_z - \frac{\bar{\phi}\boldsymbol{g}}{\gamma P^{1-1/\gamma}}\right)\right) - P^{1/\gamma}(S - \bar{S}). \tag{3.11}$$

This differs from the equation currently solved in MAESTROeX because of the $\bar{\phi}$ term, which arises because of the additional $\bar{\lambda}$ term in the momentum (3.1). To solve this equation using the existing MAESTROeX algorithm, we can use an 'old' value for $\bar{\phi}$ and, if desired, iterate to convergence. We then update λ and use (3.6) to obtain the corrected velocity, $\boldsymbol{u}$. The boundary conditions for (3.11) are chosen such that the corrected velocity satisfies the impenetrable boundary conditions. However, the solution for ϕ is then determined only up to a constant, which is a consequence of the degeneracy of the velocity constraint for impenetrable boundary conditions. The value of this constant is not arbitrary, because it affects the updated value of λ, and hence the temperature. To determine this constant, we return to the point mentioned in § 2.4, that μ should vanish on both of the impenetrable horizontal boundaries. Since $\partial\mu/\partial z = \bar{\lambda}$, this condition requires that the domain integral (or domain average) of λ must be zero, and so the domain average of $\Delta\lambda \propto \phi/P^{1-1/\gamma}$ must be zero also. In this way, the appropriate solution of (3.11) can be determined uniquely.

4. Numerical tests

We have implemented the above solution procedure into a fork of the MAESTROeX code at version 21.06. (The fork of the code can be found at https://github.com/asnodin/MAESTROeX-hybrid.) Here we compare results obtained using this implementation, in a number of test problems, with results obtained using the existing pseudo-incompressible implementation in MAESTROeX (Fan *et al.* 2019*a*) and the fully compressible CASTRO code (Almgren *et al.* 2010). To demonstrate the effect of each of our separate changes to the model, we consider four levels of refinement: M_0 denotes the original implementation; M_1, as M_0, but including the $\dot{P}_b$ term; M_2, as M_1, but including the $\bar{\lambda}$ term in the momentum equation; and M_3, as M_2, but also using the thermodynamically

consistent T, rather than T_{EoS}. Results from CASTRO are denoted with a C. Unless otherwise specified, all tests here are for an ideal gas with $\gamma = 5/3$ in a two-dimensional Cartesian box of size $L_x \times L_z$, with periodic boundary conditions in the horizontal (x) direction and impenetrable upper and lower boundaries in the vertical (z) direction. The comparison with model M_0 is complicated by the fact that, with the $\dot{P}_b$ term omitted, it is not possible to satisfy the velocity constraint (3.4) exactly for impenetrable boundary conditions. Moreover, because the value of $\dot{P}_b$ in this model is not calculated, the pressure on the lower boundary is simply held fixed. We note that MAESTROeX provides several methods for calculating the temperature, for example by solving an auxiliary equation for the specific enthalpy, H, or specific internal energy, U. To avoid potential inconsistencies, in all of our results using MAESTROeX the quantity T_{EoS} is derived from P and ρ. In Appendix B we present evolution equations for H and U that are consistent with our model M_3. Unless otherwise specified, our results are presented in c.g.s. units, which are the default in MAESTROeX.

4.1. *Internal gravity waves*

We consider perturbations to an atmosphere that is initially isothermal and in hydrostatic equilibrium. The domain has size $L_x = L_z = L = 10^9$ cm, and a numerical resolution of 64×64 cells. The initial density field is

$$\rho(t = 0) = \rho_0 e^{-z/L} + 0.1\rho_0 \exp\left(-\frac{z}{2L}\right) \cos\left(\frac{m\pi x}{L}\right) \sin\left(\frac{n\pi z}{L}\right), \qquad (4.1)$$

where $\rho_0 = 1/3 \, \mathrm{g\,cm^{-3}}$, $m = 4$ and $n = 2$. The initial pressure is calculated assuming hydrostatic balance, with uniform gravity $g = -3 \times 10^4 \, \mathrm{cm\,s^{-2}}$, and bottom pressure $P_b = 10^{13} \, \mathrm{dyn\,cm^{-2}}$. The form of the perturbation has been chosen to match a single eigenmode of the linearised equations. For a small-amplitude perturbation, we would therefore expect to see an oscillation with frequency ω given by the dispersion relation

$$\omega^2 = \frac{m^2}{m^2 + n^2 + 1/4\pi^2} N^2, \qquad (4.2)$$

where $N^2 = (\gamma - 1)(-g)/(\gamma L)$ is the Brunt–Väisälä frequency. We have chosen a relatively large amplitude for the perturbation in order to test the conservation of energy, which means that the waves break after only a few oscillation periods, $t_0 = 2\pi/\omega$. We integrate the adiabatic equations up to $t = 7t_0$ for models M_0, M_1 and M_2. (Since this test is adiabatic, model M_3 is identical to M_2.) Time series of the energy in each simulation are plotted in figure 1. In model M_0, the total energy oscillates significantly, by an amount comparable to the oscillation in the individual contributions from internal, kinetic and gravitational potential energy. By contrast, in models M_1 and M_2 the total energy is fairly well conserved, to within approximately 0.01 % while the waves remain essentially linear, and approximately 0.1 % once wave breaking occurs, at which point numerical dissipation becomes significant. The flow in all three cases is very similar, and the main difference is in the internal energy, as shown in figure 1(*a*,*b*). In this test, models M_1 and M_2 produce very similar results, indicating that the $\bar{\lambda}$ term in the momentum equation has a negligible effect. This is perhaps unsurprising given that the horizontally averaged flow is very weak in this case. The spurious oscillations in the internal energy in model M_0 result from the imposition of constant boundary pressure, which is relaxed in model M_1.
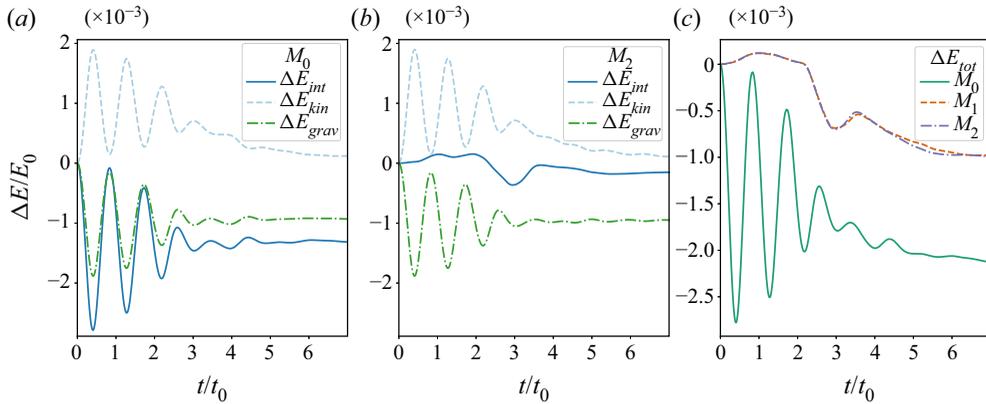
Figure 1. Time series of internal energy (E_{int}), kinetic energy (E_{kin}) and gravitational potential energy (E_{grav}) in the internal gravity wave test, for models M_0 (a) and M_2 (b). Each plot shows the change relative to the initial value as a fraction of the total initial energy. Plots for model M_1 (not shown) are very similar to those in (b). (c) The evolution of the total energy in models M_0, M_1 and M_2.

4.2. Rayleigh–Taylor instability

For this test, we begin with a layer of fluid with density ρ_1 overlaid by a layer with density $\rho_2 > \rho_1$. The entire domain is initially hydrostatic, with a piecewise linear pressure profile. Following the procedure described in Almgren *et al.* (2010), the density interface is then slightly smoothed and perturbed, with

$$\rho(x, z) = \rho_1 + \frac{\rho_2 - \rho_1}{2} \left[1 + \tanh\left(\frac{z - Z(x)}{w} \right) \right], \tag{4.3}$$

where w is the smoothing width and $Z(x)$ is the interface height:

$$Z(x) = \frac{L_z}{2} + A \cos\left(\frac{2\pi x}{L_x} \right). \tag{4.4}$$

We take the domain size to be $L_x \times L_z = 0.5\,\text{cm} \times 1\,\text{cm}$, with a resolution of 256×512 grid cells. We choose $\rho_1 = 1\,\text{g cm}^{-3}$, $\rho_2 = 2\,\text{g cm}^{-3}$, $w = 0.005\,\text{cm}$, $A = 0.01\,\text{cm}$, $g = -1\,\text{cm s}^{-2}$ and a bottom pressure of $P_b = 5\,\text{dyn cm}^{-2}$. This initial set-up was evolved for models C, M_0, M_1 and M_2 up to a time of $t = 10\,\text{s}$. In figure 2(a) we show contours of the density in models C and M_2 at times $t = 2$ and $3\,\text{s}$. (Model M_1 is very similar to M_2 at both of these times.) Up to time $t = 2\,\text{s}$ models C and M_2 show close agreement, but by $t = 3\,\text{s}$ the simulations diverge as secondary instabilities develop. These differences are likely explained by the different advection schemes used in the two codes (Almgren *et al.* 2010), rather than by differences in the models themselves. In fact, the qualitative agreement between models C and M_2 is surprising good, given that the Mach number reaches a maximum of around 0.7 during the simulation, because the pseudo-incompressible approximation is generally only expected to hold for low Mach number. Moreover, our hybrid model assumes that the (horizontally averaged) pressure remains in hydrostatic balance at all times, whereas in the CASTRO simulation there are inversions in the horizontally averaged pressure profile, as shown in figure 2(b). The pressure profiles in models M_1 and M_2 are essentially identical, whereas model M_0 has a significantly lower pressure, as a result of its pressure being fixed at the lower boundary. Models M_1 and M_2 conserve the total energy to within approximately 0.1 %, as shown in

936 A14-13
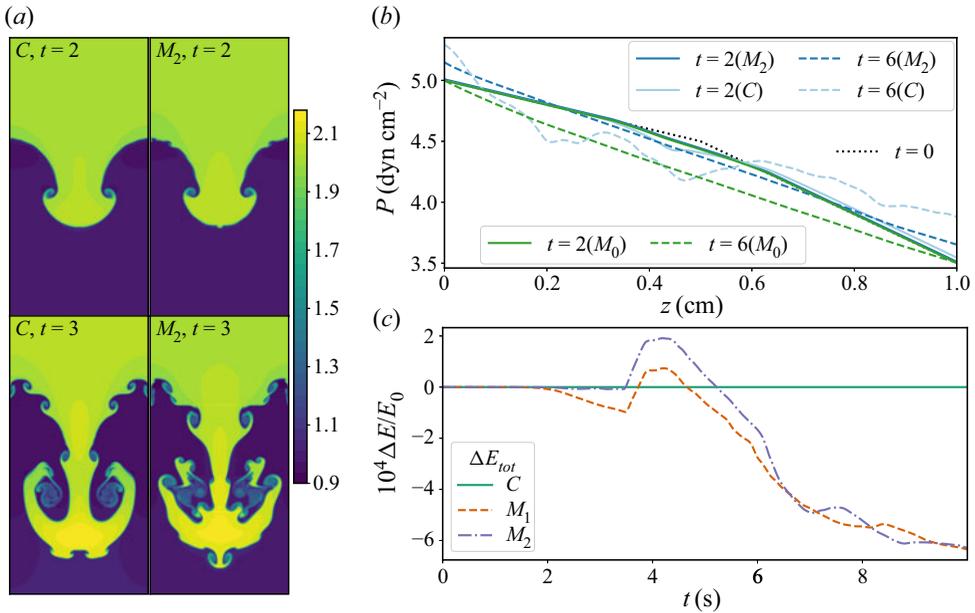
Figure 2. Contour plots of density (in $\mathrm{g\,cm^{-3}}$) in the Rayleigh–Taylor test for models C and M_2 at two times (*a*). The two simulations remain in close agreement until $t = 2\,\mathrm{s}$, but then diverge as secondary instabilities develop. At the same time, pressure inversions appear in the horizontally averaged pressure in model C (*b*), whereas the pressure in model M_2 is hydrostatic and therefore monotonic. In model M_0, which omits the $\dot{P}_b$ term, the pressure remains fixed at the upper and lower boundaries. (*c*) The evolution of the total energy in models C, M_1 and M_2.

figure 2(*c*), whereas in model M_0 the energy change is about an order of magnitude larger, and is therefore not shown.

Despite the eventual divergence of solutions between models C, M_1 and M_2, we observe quite similar energy evolution, as shown in figure 3. Model M_2 exhibits slightly better agreement with model C, although there are more significant oscillations in the gravitational and kinetic energy in model C. As shown in figure 2(*c*), model M_2 maintains better energy conservation than model M_1 up to approximately $t = 3.5\,\mathrm{s}$, at which point the Mach number reaches $Ma \simeq 0.4$. This suggests slightly better energy conservation when we include the $\bar{\lambda}$ term in our equations.

4.3. *Rising and falling bubbles in an atmosphere*

The test cases considered so far were adiabatic, and so the 'thermodynamically consistent' expression for the temperature, used in model M_3, had no effect on the results. We now present a test case involving both prescribed heat sources and thermal diffusion, in order to elucidate the effect of this change on the model. For this case the total heating, Q, has the form

$$Q = \nabla \cdot (K\nabla T) + \Pi_{t_0,t_1}(t)f(x,z), \tag{4.5}$$

where K is the thermal conductivity, which we take to be constant, and Π_{t_0,t_1} is the boxcar function, meaning that external heating is applied only for $t_0 \leqslant t \leqslant t_1$. By default, thermal diffusion is implemented in MAESTROeX in terms of the specific enthalpy (Malone *et al.* 2011), but for this test case we use the alternative implementation in terms of temperature, so that we can work with the corrected temperature, T, rather than T_{EoS}. This is important
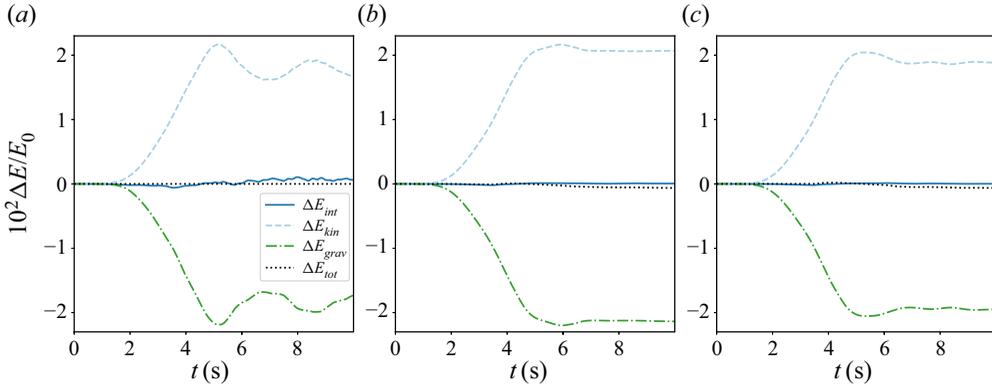
Figure 3. Evolution of energy contributions (as described in figure 1) in the Rayleigh–Taylor test for (*a*) model C, (*b*) model M_1 and (*c*) model M_2.

because, when the heating (4.5) is introduced into the heat equation (2.33), we find that

$$\frac{\partial}{\partial t}(\rho s) + \nabla \cdot (\rho s \boldsymbol{u} - K \nabla \ln T) = K|\nabla \ln T|^2 + \frac{1}{T}\Pi_{t_0,t_1}(t)f(x, z). \qquad (4.6)$$

So thermal diffusion introduces a positive-definite source of entropy, consistent with the second law of thermodynamics.

The initial pressure and density are chosen to be

$$P = P_0 \left(1 - z/L\right)^{\gamma/(\gamma-1)}, \quad \rho = \frac{1}{g}\frac{\mathrm{d}P}{\mathrm{d}z}, \qquad (4.7a,b)$$

which implies that the initial temperature, $T \propto P/\rho$, is linear in z and the initial specific entropy, $s \propto \ln(P/\rho^\gamma)$, is constant. This background state is chosen because it is steady and marginally stable to convection. The temperature gradient is fixed to its initial value at the top and bottom boundaries, so that there is no net heat flux into the domain. We use a domain of size $L_x = L_z = 2\,\mathrm{cm}$, with 1024×1024 grid cells. The parameter values are set as $L = 2.5\,\mathrm{cm}$, $P_0 = 1.65 \times 10^6\,\mathrm{dyn\,cm^{-2}}$, $g = -1 \times 10^9\,\mathrm{cm\,s^{-2}}$ and $K = 4 \times 10^4\,\mathrm{erg\,K^{-1}\,cm^{-1}\,s^{-1}}$.

The form of the heating function, $f(x, z)$, is chosen to produce a number of positively or negatively buoyant 'bubbles', via localised heat sources:

$$f(x, z) = \sum_i A_i \left(1 + \tanh(2 - |\boldsymbol{x} - \boldsymbol{x}_i|/w_i)\right), \qquad (4.8)$$

with the ith source centred at $\boldsymbol{x}_i$, with a width w_i and an amplitude A_i.

We first consider the case of a single rising bubble, by taking $\boldsymbol{x}_1 = (1, 0.7)\,\mathrm{cm}$, $A_1 = 1 \times 10^{13}\,\mathrm{erg\,cm^{-3}\,s^{-1}}$ and $w_1 = 0.025\,\mathrm{cm}$. This heating is applied between $t_0 = 1 \times 10^{-5}\,\mathrm{s}$ and $t_1 = 2 \times 10^{-5}\,\mathrm{s}$. Figure 4 shows close-ups of the bubble at $t = 2 \times 10^{-4}\,\mathrm{s}$, for models M_2, M_3 and C; this is the time at which differences between the simulations became measurable. We do not present results from model M_1 because in that simulation the velocity projection failed to converge, which suggests that the $\bar{\lambda}$ term in the momentum equation is essential to this test case. Figure 4(*a*–*c*) shows temperature contours for each model; the contours for model C are slightly sharper, which we attribute to the different advection scheme used in CASTRO because all of the models have the same thermal conductivity. The differences between the models are made clearer by plotting the relative
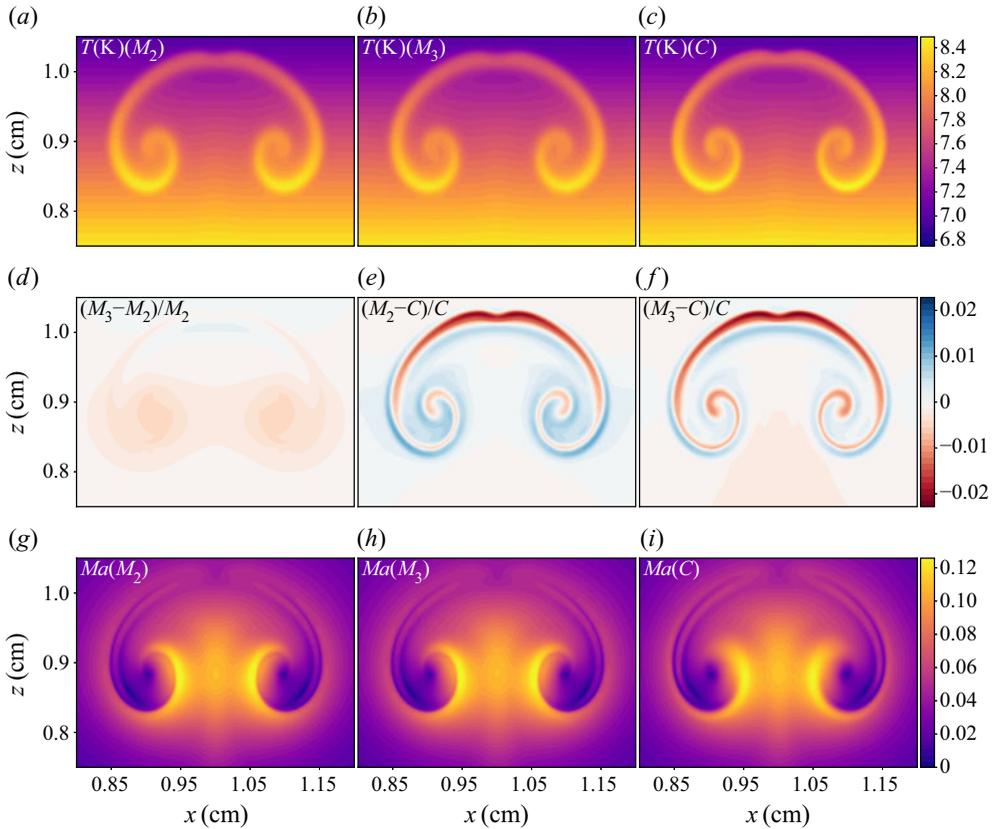
Figure 4. Contour plots of temperature for a single rising bubble at $t = 2 \times 10^{-4}$ s for cases M_2, M_3 and C (*a–c*). (*d–f*) Relative temperature differences between plots in (*a–c*) as indicated in each panel. (*g–i*) Contours of Mach number corresponding to the cases as in (*a–c*).

temperature differences, as is done in figure 4(*d–f*). We see that the temperature correction introduced in model M_3 is positive in the vicinity of the bubble, making that bubble slightly more buoyant compared to model M_2. This correction to the temperature also produces a better agreement between models M_3 and C. Figure 4(*g–i*) shows the local Mach number in the three models, which all agree to within 1 %.

Figure 5 shows time series of energy in the same simulations. After the initial injection of heat, the total energy is conserved almost perfectly in model C and to within 0.001 % in models M_2 and M_3. Cases M_2 and M_3 are essentially indistinguishable; in both cases the gravitational potential energy steadily decreases as the bubble rises, leading to an increase in kinetic energy and internal energy (through dissipative heating). The kinetic energy in model C follows a very similar trajectory, as expected given the similarities in the flow seen in figure 4. However, the internal and gravitational energy terms in model C exhibit a more dramatic, quasi-periodic oscillation, which we attribute to lack of hydrostatic balance in the horizontally averaged dynamics. The injection of heat in this fully compressible model establishes a gentle vertical 'sloshing' that is associated with very small velocities yet large changes in the internal and gravitational energy terms. In an attempt to reduce this effect, and allow a more meaningful comparison with model C, we have considered a second configuration with one rising bubble and one sinking bubble, as illustrated in figure 6. For this case, we place heat sources at $x_+ = (2/3, 1)$ cm and $x_- = (4/3, 1)$ cm,

936 A14-16
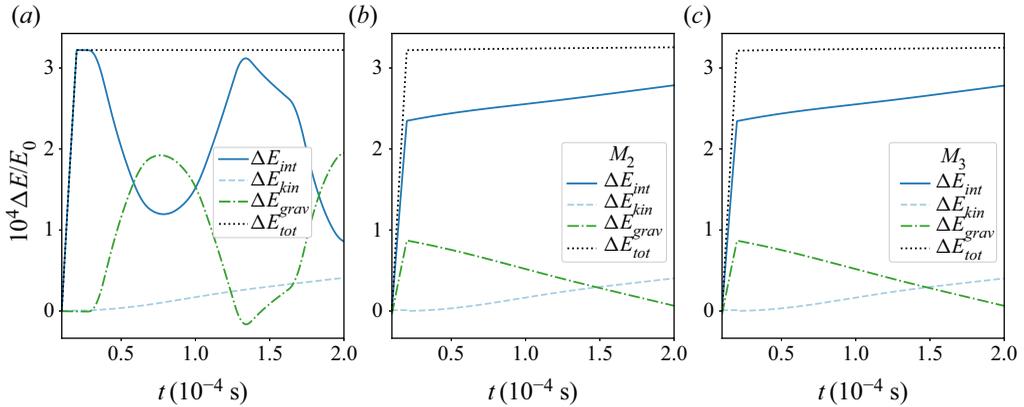
Figure 5. Evolution of the energy for the single rising bubble test for case C (*a*), case M_2 (*b*) and case M_3 (*c*). The plotted components are as described in figure 1. The time axis starts at $t = 1 \times 10^{-5}$ s, when the heating is turned on.
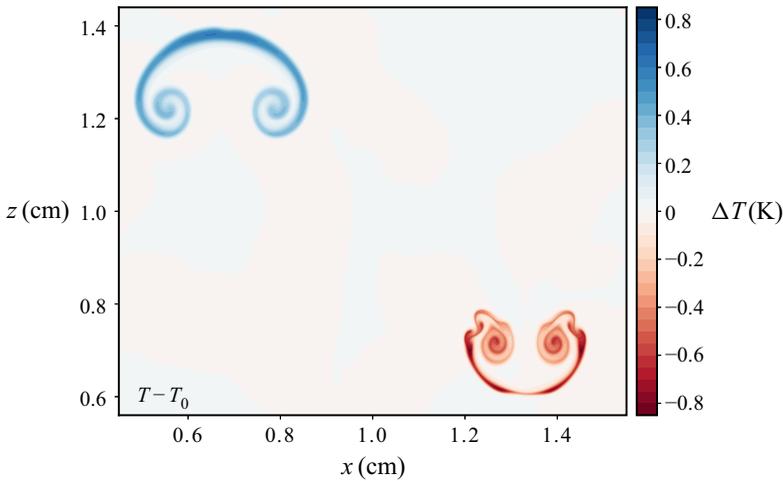
Figure 6. The temperature at $t = 1.9 \times 10^{-4}$ s, minus the initial temperature, in the two-bubble test with model C. (The results of models M_2 and M_3 are very similar.)

with amplitudes $A = \pm 2 \times 10^{13}$ erg cm^{-3} s^{-1} and the same width $w = 0.025$ cm. These heat sources are both applied between $t_0 = 1 \times 10^{-5}$ s and $t_1 = 7 \times 10^{-5}$ s. For these simulations we use a numerical resolution of 512×512 grid cells. The energy evolution for this configuration is shown in figure 7 for models C, M_2 and M_3. We note that the heat source and sink are not implemented exactly symmetrically, and so there is a slight drop in the total energy between times t_0 and t_1. However, after this time the total energy is conserved just as well as in the single bubble case. There are still significant fluctuations in the gravitational and internal energy in model C, but these are of much lower amplitude than in the single bubble case. Models M_2 and M_3 again produce very similar results, although both have a slightly lower kinetic energy than model C. In model C, as shown in figure 7(*a*), the gravitational potential energy remains nearly constant until $t \simeq 3 \times 10^{-5}$ s, which is roughly equal to the sound-crossing time in the domain. Up to this time, the imposed heating produces an increase in the local fluid pressure without much change in
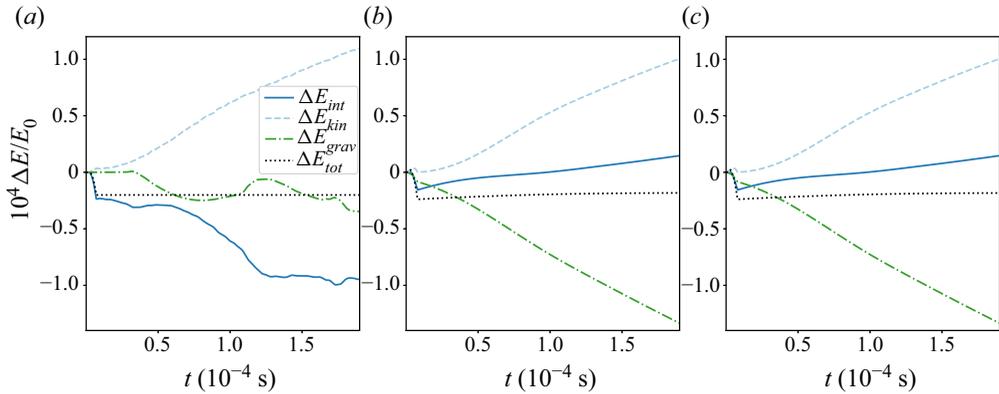
Figure 7. Evolution of the energy as in figure 5, but for the rising and falling bubble test.

density. In models M_2 and M_3, by contrast, the imposed heating produces an instantaneous expansion or contraction of the fluid, as dictated by the velocity constraint (3.4).

5. Summary and discussion

By formulating an appropriate action, we have derived a hybrid pseudo-incompressible–hydrostatic model that conserves energy. In the case of closed boundaries, the velocity must satisfy a degenerate constraint equation, and this degeneracy is broken by requiring that the energy flux through the boundaries vanishes. We have implemented this model within the existing MAESTROeX framework and validated it in a number of test cases, including comparison with results from the fully compressible code CASTRO. Our changes to the MAESTROeX algorithm generally have a small effect on the numerical results, but in at least some cases they produce better energy conservation and better agreement with the fully compressible code. The main benefit of using a sound-proof model is that larger time steps can be used. For example, in the case shown in figure 4, we used a time step of 3.28×10^{-7} s, whereas CASTRO required a time step of 3.34×10^{-8} s, a factor of 10 smaller. In our test cases the Mach number was typically $Ma \simeq 0.5$, whereas in many practical applications one would have $Ma \ll 1$, in which case a sound-proof model becomes much more efficient, as well as more accurate. Of course, the time step may still be limited by other factors, such as the presence of high-frequency internal gravity waves (Higl, Müller & Weiss 2021). In such cases, other numerical techniques such as Runge–Kutta time integration may lead to greater numerical stability.

Although we have chosen to focus on the case of closed boundary conditions, the approach we have outlined can also be applied to the case of 'open' boundary conditions. If either the lower or upper boundary is open then the background pressure should be evolved according to (2.37) but with the $\dot{P}_b$ term set to zero, as is already implemented in MAESTROeX. As mentioned in § 2.4, this ensures that there are no unphysical boundary fluxes associated with the Lagrange multiplier μ. For similar reasons, the other Lagrange multiplier, λ, should be set to zero on any open boundaries; this also removes any degeneracy when calculating the velocity correction.

All of the numerical test cases we have presented here involve a single (ideal) gas, but MAESTROeX is designed for multi-fluid applications with complex reaction networks. In such applications the reaction rates are often very temperature-sensitive, and we plan to test whether using the corrected temperature, rather than T_{EoS}, produces more accurate results.

936 A14-18

Declaration of interests. The authors report no conflict of interest.

Data availability statement. Data used to produce figures can be found at https://doi.org/10.25405/data.ncl.c.5752439.

Author ORCIDs.

 A.P. Snodin https://orcid.org/0000-0001-7551-3511;

 T.S. Wood https://orcid.org/0000-0003-1044-170X.

Appendix A. Unsplit velocity projection

We would like to solve the equation

$$\nabla \cdot \left(\frac{P^{2/\gamma}}{\rho} \nabla \phi \right) - \frac{(\gamma - 1)gP^{2/\gamma}}{\gamma^2 P^2} \frac{\partial P}{\partial z} \bar{\phi} = \nabla \cdot (P^{1/\gamma} \boldsymbol{u}^\dagger) - \frac{gP^{1/\gamma}}{\gamma P} \overline{\rho u_z^\dagger} - \frac{\gamma PS - \dot{P}_b}{\gamma P^{1-1/\gamma}} \tag{A1}$$

subject to the boundary condition

$$\frac{1}{\rho} \frac{\partial \phi}{\partial z} + \frac{g\bar{\phi}}{\gamma P} = P^{-1/\gamma} u_z^\dagger \tag{A2}$$

on the upper and lower boundaries, which is obtained via (3.6), taking $\boldsymbol{u}$ to satisfy the impenetrable boundary condition.

We consider the adjoint of (A1), using $\phi^\dagger$ to denote the adjoint variable. Since the operator on the left-hand side of this equation is self-adjoint with respect to the usual L^2-norm, the adjoint problem is simply the homogeneous version of (A1)–(A2):

$$\nabla \cdot \left(\frac{P^{2/\gamma}}{\rho} \nabla \phi^\dagger \right) - \frac{(\gamma - 1)gP^{2/\gamma}}{\gamma^2 P^2} \frac{\partial P}{\partial z} \overline{\phi^\dagger} = 0, \tag{A3}$$

with boundary condition

$$\frac{1}{\rho} \frac{\partial \phi^\dagger}{\partial z} + \frac{g\overline{\phi^\dagger}}{\gamma P} = 0. \tag{A4}$$

The solution of this adjoint problem is unique, up to a constant multiplicative factor. Multiplying (A1) by this solution, integrating by parts and applying the boundary conditions for ϕ and $\phi^\dagger$, we eventually obtain the solvability condition

$$\int \left[\boldsymbol{u}^\dagger \cdot \nabla \phi^\dagger + \frac{g}{\gamma P} \overline{\rho u_z^\dagger} \phi^\dagger + S\phi^\dagger \right] P^{1/\gamma} \, \mathrm{d}^3\boldsymbol{x} = \dot{P}_b \int \frac{\phi^\dagger}{\gamma P^{1-1/\gamma}} \, \mathrm{d}^3\boldsymbol{x}. \tag{A5}$$

Therefore, assuming that the adjoint solution $\phi^\dagger$ can be computed, the necessary value for $\dot{P}_b$ can be expressed as the ratio of two domain integrals. We recover our result (3.10) if we approximate $\phi^\dagger \simeq P^{-1/\gamma}$ and $\tilde{u}_z^\dagger = \tilde{u}_z$; these approximations become exact if ρ happens to be a function of z only, in which case we recover the formula (2.40) of O'Neill & Klein (2014).

For this value of $\dot{P}_b$, (A1) can be solved for ϕ, up to an arbitrary multiple of $\phi^\dagger$. As in § 3, this remaining degeneracy is removed by the requirement that the domain average of $\phi/P^{1-1/\gamma}$ must be zero.

Appendix B. Auxiliary evolution equations

The general hybrid equations (2.31)–(2.34) can be used to obtain evolution equations for other thermodynamic quantities, e.g. the specific internal energy, $U(\rho, s)$, or the specific enthalpy, $H = U + P/\rho$:

$$\rho \frac{\mathrm{D}U}{\mathrm{D}t} = -P\nabla \cdot \boldsymbol{u} + \frac{T_{EoS}}{T}Q, \tag{B1}$$

$$\rho \frac{\mathrm{D}H}{\mathrm{D}t} = \frac{\mathrm{D}P}{\mathrm{D}t} + \frac{T_{EoS}}{T}Q. \tag{B2}$$

We note that, in both cases, the applied heating, Q, must be multiplied by the correction factor T_{EoS}/T.

REFERENCES

ALMGREN, A.S. 2000 A new look at the pseudo-incompressible solution to Lamb's problem of hydrostatic adjustment. *J. Atmos. Sci.* **57** (7), 995–998.

ALMGREN, A.S., BECKNER, V.E., BELL, J.B., DAY, M.S., HOWELL, L.H., JOGGERST, C.C., LIJEWSKI, M.J., NONAKA, A., SINGER, M. & ZINGALE, M. 2010 CASTRO: a new compressible astrophysical solver. I. Hydrodynamics and self-gravity. *Astrophys. J.* **715** (2), 1221–1238.

ALMGREN, A.S., BELL, J.B. & CRUTCHFIELD, W.Y. 2000 Approximate projection methods: part I. Inviscid analysis. *SIAM J. Sci. Stat. Comput.* **22** (4), 1139–1159.

ALMGREN, A.S., BELL, J.B., NONAKA, A. & ZINGALE, M. 2008 Low Mach number modeling of type Ia supernovae. III. Reactions. *Astrophys. J.* **684** (1), 449–470.

ARAKAWA, A. & KONOR, C.S. 2009 Unification of the anelastic and quasi-hydrostatic systems of equations. *Mon. Weath. Rev.* **137** (2), 710–726.

BRETHERTON, F.P. 1970 A note on Hamilton's principle for perfect fluids. *J. Fluid Mech.* **44**, 19–31.

DAVIES, T., STANIFORTH, A., WOOD, N. & THUBURN, J. 2003 Validity of anelastic and other equation sets as inferred from normal-mode analysis. *Q. J. R. Meteorol. Soc.* **129** (593), 2761–2775.

DUBOS, T. & VOITUS, F. 2014 A semihydrostatic theory of gravity-dominated compressible flow. *J. Atmos. Sci.* **71** (12), 4621–4638.

DURRAN, D.R. 1989 Improving the anelastic approximation. *J. Atmos. Sci.* **46** (11), 1453–1461.

DURRAN, D.R. 2008 A physically motivated approach for filtering acoustic waves from the equations governing compressible stratified flow. *J. Fluid Mech.* **601**, 365–379.

FAN, D., NONAKA, A., ALMGREN, A.S., HARPOLE, A. & ZINGALE, M. 2019*a* MAESTROeX: a massively parallel low Mach number astrophysical solver. *Astrophys. J.* **887** (2), 212.

FAN, D., NONAKA, A., ALMGREN, A.S., WILLCOX, D., HARPOLE, A. & ZINGALE, M. 2019*b* MAESTROeX: a massively parallel low mach number astrophysical solver. *J. Open Source Softw.* **4** (43), 1757.

GAY-BALMAZ, F. 2019 A variational derivation of the thermodynamics of a moist atmosphere with rain process and its pseudoincompressible approximation. *Geophys. Astrophys. Fluid Dyn.* **113** (5–6), 428–465.

GOFFREY, T., PRATT, J., VIALLET, M., BARAFFE, I., POPOV, M.V., WALDER, R., FOLINI, D., GEROUX, C. & CONSTANTINO, T. 2017 Benchmarking the multidimensional stellar implicit code MUSIC. *Astron. Astrophys.* **600**, A7.

HIGL, J., MÜLLER, E. & WEISS, A. 2021 Calibrating core overshooting parameters with two-dimensional hydrodynamical simulations. *Astron. Astrophys.* **646**, A133.

KLEIN, R. & PAULUIS, O. 2012 Thermodynamic consistency of a pseudoincompressible approximation for general equations of state. *J. Atmos. Sci.* **69** (3), 961–968.

LECOANET, D., BROWN, B.P., ZWEIBEL, E.G., BURNS, K.J., OISHI, J.S. & VASIL, G.M. 2014 Conduction in low Mach number flows. I. Linear and weakly nonlinear regimes. *Astrophys. J.* **797** (2), 94.

MALONE, C.M., NONAKA, A., ALMGREN, A.S., BELL, J.B. & ZINGALE, M. 2011 Multidimensional modeling of type I X-ray Bursts. I. Two-dimensional convection prior to the outburst of a pure ^{4}He accretor. *Astrophys. J.* **728** (2), 118.

MILLER, M.J. & PEARCE, R.P. 1974 A three-dimensional primitive equation model of cumulonimbus convection. *Q. J. R. Meteorol. Soc.* **100** (424), 133–154.

NEWCOMB, W.A. 1962 Lagrangian and Hamiltonian methods in magnetohydrodynamics. *Nucl. Fusion Suppl.* **2**, 451–463.

O'NEILL, W.P. & KLEIN, R. 2014 A moist pseudo-incompressible model. *Atmos. Res.* **142**, 133–141.

REHM, R.G. & BAUM, H.R. 1978 Equations of motion for thermally driven, buoyant flows. *J. Res. Natl Bur. Stand.* **83** (3), 297–308.

SALMON, R. 1982 Hamilton's principle and Ertel's theorem. In *Mathematical Methods in Hydrodynamics and Integrability in Dynamical Systems* (ed. M. Tabor & Y.M. Treve), Am. Inst. Phys. Conf. Proc., vol. 88, pp. 127–135. American Institute of Physics.

SALMON, R. 1988 Hamiltonian fluid mechanics. *Annu. Rev. Fluid Mech.* **20**, 225–256.

SALMON, R. & SMITH, L.M. 1994 Hamiltonian derivation of the nonhydrostatic pressure-coordinate model. *Q. J. R. Meteorol. Soc.* **120** (519), 1409–1413.

VASIL, G.M., LECOANET, D., BROWN, B.P., WOOD, T.S. & ZWEIBEL, E.G. 2013 Energy conservation and gravity waves in sound-proof treatments of stellar interiors. II. Lagrangian constrained analysis. *Astrophys. J.* **773** (2), 169.

VIALLET, M., GOFFREY, T., BARAFFE, I., FOLINI, D., GEROUX, C., POPOV, M.V., PRATT, J. & WALDER, R. 2016 A Jacobian-free Newton-Krylov method for time-implicit multidimensional hydrodynamics. Physics-based preconditioning for sound waves and thermal diffusion. *Astron. Astrophys.* **586**, A153.

WHITE, A.A. 1989 An extended version of a nonhydrostatic, pressure coordinate model. *Q. J. R. Meteorol. Soc.* **115** (490), 1243–1251.